Intermetallic Nanocatalyst for Highly Active Heterogeneous Hydroformylation

Minda Chen,¹ Geet Gupta,² Claudio W. Ordonez,¹ Andrew R. Lamkins,¹ Charles J. Ward,¹ Celia A. Abolafia,¹ Biying Zhang,¹ Luke T. Roling,²* Wenyu Huang¹,³*

ABSTRACT: Hydroformylation is an imperative chemical process traditionally catalyzed by homogeneous catalysts. Designing a heterogeneous catalyst with high activity and selectivity in hydroformylation is challenging but essential to allow the convenient separation and recycle of precious catalysts. Here, we report the development of an outstanding catalyst for efficient heterogeneous hydroformylation, RhZn intermetallic nanoparticles. In the hydroformylation of styrene, it shows three times higher turnover frequency (3090 h^{-1}) compared to the benchmark homogeneous Wilkinson's catalyst (966 h^{-1}), as well as a high chemoselectivity towards aldehyde products. RhZn is active for a variety of olefin substrates and can be recycled without a significant loss of activity. Density functional theory calculations show that the RhZn surfaces reduce the binding strength of reaction intermediates and have lower hydroformylation activation energy barriers compared to pure Rh(111), leading to more favorable reaction energetics on RhZn. The calculations also predict potential catalyst design strategies to achieve high regioselectivity.

INTRODUCTION

Hydroformylation of olefins to produce C+1 aldehydes is an essential chemical process as it involves the atom-economic formation of a C-C bond. Since its discovery as "the oxo process", hydroformylation has been developed into one of the largest-scale catalytic reactions in the chemical industry, generating over 10 million tons of products annually. Naturally, the addition of the formyl group occurs at either side of the olefin double bond during the hydroformylation process, yielding a mixture of linear and branched aldehydes, in which the linear one is typically preferred. Numerous efforts have been devoted to designing catalysts for improved activity and regioselectivity of hydroformylation. In particular, organometallic Rh complexes with various triphenylphosphine ligands have shown excellent activity and linear aldehyde selectivity.²⁻⁴ Although well-studied and highly performing, these homogeneous catalysts generally have limited recyclability that constrains their applications, considering the high cost of Rh. Therefore, heterogeneous catalysts are considered a promising alternative for hydroformylation reac-

Metallic Rh nanoparticles, unsupported 5 or supported (e.g., C, 6 TiO₂, 7 SiO₂, 8 ZIF-8, 9 zeolites 10), have been explored as candidates for heterogenized hydroformylation and are reported active for a variety of olefin substrates. However, their catalytic activity and linear aldehyde selectivity are uncompetitive compared to homogeneous catalysts. With the recent development of single-atom-catalysts (SACs), isolated Rh atoms supported on ZnO 11 and CoO 12 are found to be highly active for hydroformylation. Wang and co-workers showed that the Rh₁/CoO catalyst is active towards hydroformylation of propene with >90% selectivity towards the linear aldehyde. These results demonstrate SACs as an effective way to bridge

heterogeneous and homogeneous catalysis. However, synthesizing SACs with high metal loading and maintaining stability under high temperatures remain challenging.

Intermetallic nanoparticles (iNPs) are unique catalytic platforms known for outstanding catalytic performance in various chemical transformations. 13-20 Inactive metals provide geometric and/or electronic modification to the active metal sites (e.g., Pt/Pd/Rh) so that molecule adsorption behavior is drastically different from corresponding monometallic surfaces. This effect enables effective environment control of the catalytic active site and is analogous to the SACs in terms of site isolation. For example, Feng and co-workers have demonstrated with PdIn iNPs that the isolated Pd sites on PdIn(110) surface exhibit a superior hydrogenation selectivity compared to ensembled Pd sites.²¹ Similarly, the isolated Pd sites on PdSn iNPs lead to selectivity hydrogenation of C=O over C=C bond in α,β -unsaturated aldehydes.²² Site isolation also leads to increased diffusion barrier of hydrogen atoms on intermetallic surface, which enhances selectivity in the pairwise hydrogenation of alkene²³ and alkynes.²⁴ Additionally, the intermetallic structures are thermodynamically stable and thus often resistant to catalytic deactivation associated with high-temperature sintering, 25 coking, 26 or CO-poisoning. 27 These features make Rh-based iNPs good candidates for heterogeneous hydroformylation.

In this work, we report RhZn iNPs supported on mesoporous silica (SBA-15) as a highly active heterogeneous catalyst in hydroformylation reaction. Using styrene as a model substrate, RhZn iNPs outperform monometallic Rh nanoparticles and the benchmark homogeneous Wilkinson's catalyst, RhCl(PPh₃) $_3$. A substrate scope study demonstrates the excellent activity of RhZn iNPs in the hydroformylation of a variety of olefins. We utilize density functional

¹Department of Chemistry, Iowa State University, Ames, IA 50011, United States

²Department of Chemical and Biological Engineering, Iowa State University, Ames, IA 50011, United States

³Ames Laboratory, U.S. Department of Energy, Ames, IA 50011, United States

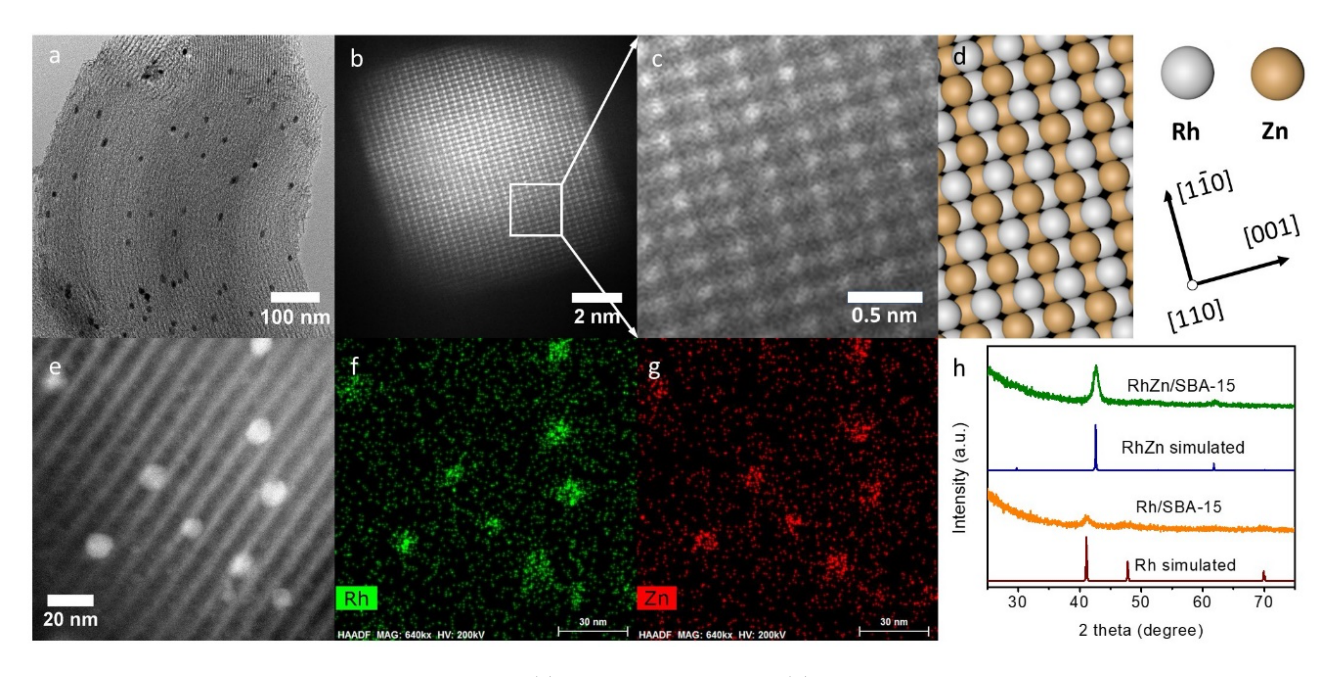


Figure 1. Characterization of RhZn/SBA-15 nanocatalyst. (a) TEM of RhZn/SBA-15. (b) Atomic resolution STEM image of an RhZn particle at the (110) axis. (c) Enlarged STEM image and (d) the simulated model of RhZn crystal matching the image. (e)-(g) EDS elemental mapping of a RhZn particle. (h) PXRD of Rh/SBA-15 and RhZn/SBA-15.

theory (DFT) calculations of hydroformylation thermodynamics and kinetics to elucidate the detailed reactivity of several low-energy RhZn intermetallic surfaces, showing that the intermetallic RhZn structure weakens the binding of surface intermediates while lowering activation energy barriers and therefore favors a rapid reaction. A temperature-programmed CO-desorption study confirms the weakened surface CO adsorption on RhZn iNPs. These findings demonstrate the exciting potential to employ iNPs for heterogeneous hydroformylation and other reactions that remain to be heterogenized.

RESULTS AND DISCUSSION

While a tremendous amount of work has been done to study the formation process and properties of iNPs, Rh-based intermetallic phases received much less attention compared to Pt- or Pd-based intermetallic phases. The formation temperatures of intermetallic phases, usually well-described in the binary phase diagrams, are insufficiently documented or missing for many Rh-based systems (e.g., Rh-Ga, Rh-In, Rh-Zn). While this can be associated with the high cost of Rh and its less common usage than Pt- or Pd-based catalysts, fundamental studies on Rh catalysts are undoubtedly necessary for applying them to specific chemical processes such as hydroformylation.

Using an incipient wetness impregnation method, we prepared a series of Rh-based iNPs, including RhZn, Rh₃Sn₂, RhSb, RhIn, RhGa, and RhBi, supported on mesoporous silica (SBA-15). Transmission electron microscopy (TEM) image of RhZn/SBA-15 in Figure 1a shows the highly monodisperse RhZn nanoparticles distributed evenly within the SBA-15 framework. The average size of RhZn iNPs is measured to be 9.6 \pm 0.6 nm, well matching the calculated crystal domain of 9.2 nm from powder X-ray diffraction (PXRD) pattern (Figure 1h) using Scherrer equation. Atomic-resolution images taken by aberration-corrected scanning transmission electron microscopy (STEM) show the ordered structure of Rh and Zn atoms within a nanoparticle (Figure 1b-c). The particle viewed along the [110] axis shows alternating rows of Rh and Zn as brighter and darker columns,

respectively. This STEM image matches well with the crystal structure of RhZn viewed from [110] zone axis (Figure 1d). Energy-dispersive X-ray spectroscopy (EDS) mapping (Figure 1e-g) confirms the even distribution of Rh and Zn within the iNPs. Inductively coupled plasma mass spectrometry (ICP-MS) also confirms the successful loading of Rh and Zn in the catalyst (Table S1).

To understand the formation of Rh-based iNPs, we monitored the phase evolution of intermetallic RhZn, as an example, using PXRD. Using a typical pore-filling impregnation method, we first prepared Rh nanoparticles supported on SBA-15. Figure S1 and S2 show the characterization results of Rh/SBA-15 by PXRD and TEM. Then, an equimolar amount of $Zn(NO)_3$ is impregnated into Rh/SBA-15, and the subsequent reduction to form RhZn iNPs is monitored by in situ PXRD (Figure S3). In a reductive gas environment, diffraction peaks corresponding to the RhZn phase appear after the temperature reaches 350 °C, grow until 450 °C, and stay mostly unchanged at further annealing to 500 °C. No additional change of the diffraction pattern is observed while maintaining the temperature at 500 °C for 1 h and cooling down to room temperature, demonstrating RhZn as a stable intermetallic phase. Therefore, we choose 500 °C as a proper reduction temperature to obtain pure phase RhZn iNPs. Cubic-structured RhZn/RhIn/RhGa with a CsCl prototype, orthorhombic RhSb with a FeAs prototype, and hexagonal Rh₃Sn₂ with a Co_{1.75}Ge prototype are synthesized under similar conditions, whose structures are confirmed by ex-situ PXRD (Figure 1h and Figure S1).

To investigate the chemical states of Rh and Zn at the iNP surface, we conducted X-ray photoelectron spectroscopy (XPS) on freshly reduced Rh/SBA-15 and RhZn/SBA-15 catalysts (Figure S4). In the Rh 3d XPS spectra, the Rh 3d 5/2 peak at 306.6 eV was present for both Rh and RhZn, characteristic of Rh(0). Moreover, the overlapping peak position indicates that no significant electron transfer happened between Rh and Zn in RhZn iNPs, which is reasonable considering the similar absolute electronegativities of Rh and Zn.³⁰ The chemical state of Zn is less straightforward to find out. First, we see a

broadening of Zn 2p 3/2 peak at lower binding energy of ~1018 eV attributed to O Auger signal. The true Zn 2p 3/2 peak is at ~1022 eV. The chemical state of Zn, however, cannot be identified from binding energy of Zn 2p alone. One has to use the modified Auger parameter that requires scanning the Zn LM2 Auger line. The binding energy of Zn 2p plus the kinetic energy of the Zn LM2 yields a modified Auger parameter of ~2014 eV. This is consistent with Zn in the metallic state. Therefore, both Rh and Zn exist in the metallic state at the nanoparticle surface.

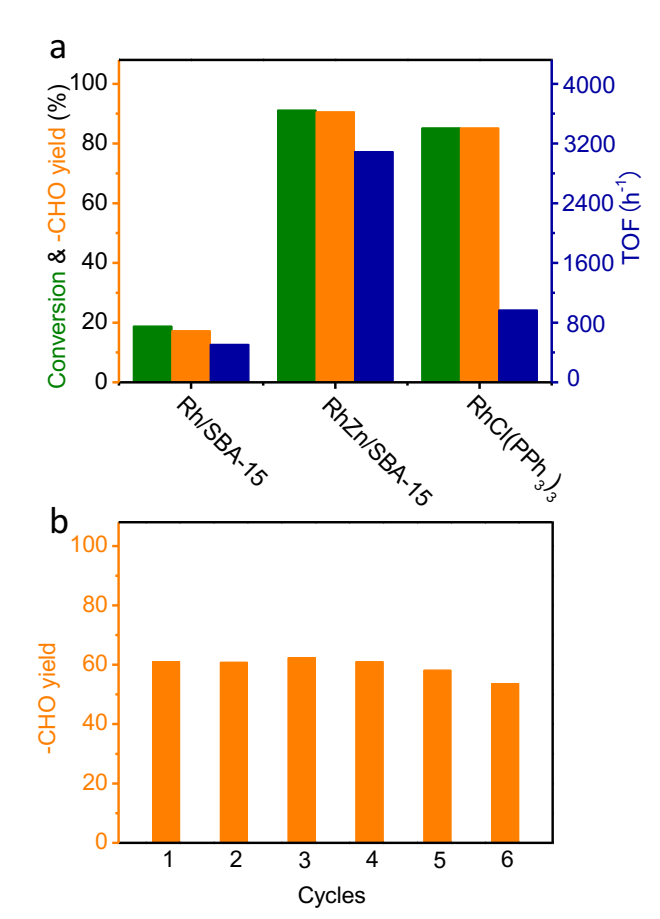


Figure 2. Test of catalytic performance on styrene hydroformylation. (a) Comparing the catalytic performance of Rh/SBA-15, RhZn/SBA-15, and RhCl(PPh₃)₃ for the hydroformylation of styrene. Reaction condition: 0.5 mmol styrene, 2.0 mL toluene, 30 bar syngas, 100 °C, 2 h. TOF of each catalyst is calculated based on the yield of aldehydes at a conversion level of ~10% using each catalyst. (b) recyclability of RhZn/SBA-15 tested over 6 cycles of styrene hydroformylation. The conversion level is maintained at around 60% during the recycling study.

Known for its high surface area, the SBA-15 support is examined by $N_2\text{-sorption}$ isotherm using the Brunauer–Emmett–Teller (BET) method (Figure S5). A surface area of $1280\pm10~\text{m}^2/\text{g}$ and a pore volume of $1.06~\text{cm}^3/\text{g}$ is obtained. After loading Rh and RhZn nanoparticles, the corresponding surface areas decline to $1030\pm10~\text{and}$ 790 \pm 10 m^2/g , respectively. The pore volumes (1.03 and 0.99 cm $^3/\text{g}$ for Rh/SBA-15 and RhZn/SBA-15, respectively) only decrease slightly compared to the value before metal loading, suggesting the porous structure of SBA-15 is preserved after loading Rh and RhZn nanoparticles.

We applied these Rh-based iNPs in the hydroformylation of styrene to evaluate their catalytic performances. Figure S6-S7 shows the

screening result of all the Rh-based iNPs synthesized. The optimized reaction condition is determined on RhZn/SBA-15 (Table S2), 30 bar CO:H $_2$ (1:1) at 100 °C in toluene. Under this condition, Rh/SBA-15 shows 17.3% yield to aldehyde products and a linear to branch (l:b) ratio of 1.1 (Table S3). Comparatively, although none of the intermetallic catalysts achieves significantly high l:b ratios, RhIn and RhZn iNPs demonstrate significantly enhanced yield from Rh. With RhZn, a yield of 90.6% to aldehydes is achieved with a l:b ratio of 1.4 within 2 h, the highest among all tested catalysts (Figure S6).

Such high activity of the RhZn catalyst motivates us to compare it with a benchmark homogeneous catalyst, Wilkinson's catalyst. Figure 2a shows a detailed performance comparison of Rh, RhZn, and Wilkinson's catalyst with the same amount of Rh (0.4 μmol). All three catalysts show excellent chemoselectivity to aldehydes, and only minor hydrogenation byproducts are generated by Rh (1.5% yield) and RhZn (0.6% yield). The yield of aldehydes from RhZn (90.6%) is slightly higher than Wilkinson's catalyst (85.2%) and is significantly higher than Rh (17.3%), again suggesting RhZn to be a superior catalyst in terms of activity. Wilkinson's catalyst gives a l:b ratio of 1.3 that is close to the values obtained from Rh and RhZn catalysts. To fairly compare the efficiency of different catalytic active sites, we calculate the turnover frequency (TOF) of each catalyst by carrying out the reactions at a low conversion level (ca. 10%). The fractions of surface Rh sites on Rh and RhZn are determined by CO chemisorption to be 11.1 and 6.1%, respectively. Since Wilkinson's catalyst is a molecular catalyst, all Rh atoms are considered to be active. Thus, we can calculate the efficiency of catalytic conversion on each active site, i.e., TOF of the catalyst. The TOF of RhZn is 3090 h⁻¹ that is more than three times higher than the TOF of Wilkinson's catalyst (966 h⁻¹) and six times higher than Rh (509 h⁻¹), confirming the outstanding performance of RhZn. A control experiment using bare SBA-15 as catalyst produces no conversion of styrene under the same condition, suggesting that the catalytic activity comes from Rh sites. Furthermore, the RhZn/SBA-15 catalyst can be recycled by centrifuging and washing with ethanol. After being reused six times (Figure 2b), no significant loss of catalytic activity is observed. The good recyclability is a major advantage of using the RhZn/SBA-15 catalyst in hydroformylation. PXRD (Figure S8) and XPS (Figure S4) of the recycled RhZn/SBA-15 catalyst show no apparent change in crystal structure of RhZn or oxidation states of constituent elements. Compared with other recently published heterogeneous hydroformylation catalysts (Table S3), such as SACs or zeolite-supported Rh nanoparticles, the RhZn intermetallic catalyst shows comparable catalytic performance, expanding the catalyst choice of heterogenized hydroformylation.

We have further explored the substrate scope of the hydroformylation reaction catalyzed by RhZn iNPs, as shown in Table 1. Substituted styrene (entry 2-3), namely 4-chlorostyrene and 3-nitrostyrene, show comparable TOF to styrene and excellent chemoselectivity. These results show the high tolerance of the RhZn/SBA-15 catalyst to -Cl and -NO2 functional groups on the substrate. In particular, with 3-nitrostyrene, where hydrogenation side reactions can happen on both the -NO2 and the olefin groups, the excellent chemoselectivity to aldehyde products was demonstrated as no hydrogenation products were detected. Substantially lower activity was observed with αmethylstyrene, consistent with previous studies, 11 likely due to the large steric hindrance near the olefin group that inhibits its adsorption on the RhZn surface. Two other common substrates, 1-hexene and 1octene, have also been tested. Lower activity was obtained, likely due to the isomerization of the terminal to internal olefins, which results in slower reaction kinetics. For each substrate, RhZn/SBA-15 has

Table 1. Substrate scope of hydroformylation with RhZn/SBA-15 nanocatalyst.

Entry	Substrate –	RhZn/SBA-15		Wilkinson's catalyst	
		TOF (h-1)	-CHO selectivity (%)	TOF (h-1)	-CHO selectivity (%)
1		3090	99.3	966	>99.9
2	CI	2513	99.5	1058	>99.9
3	NO ₂	2762	99.6	1154	>99.9
4		260	>99.9	105	>99.9
5		1341	99.7*	556	>99.9*
6	\\\\\\\\\\\\\\\\\\\\\\\\\\\\\\\\\\\\\\	1134	98.9*	473	>99.9*

Reaction conditions: 0.5 mmol olefin, 2.0 mL toluene, 30 bar CO:H₂ (1:1), 100 °C, 2 h. To calculate TOF, catalyst amounts are adjusted to control conversion level at *ca.* 10%. *Isomerized internal olefins are not counted as products.

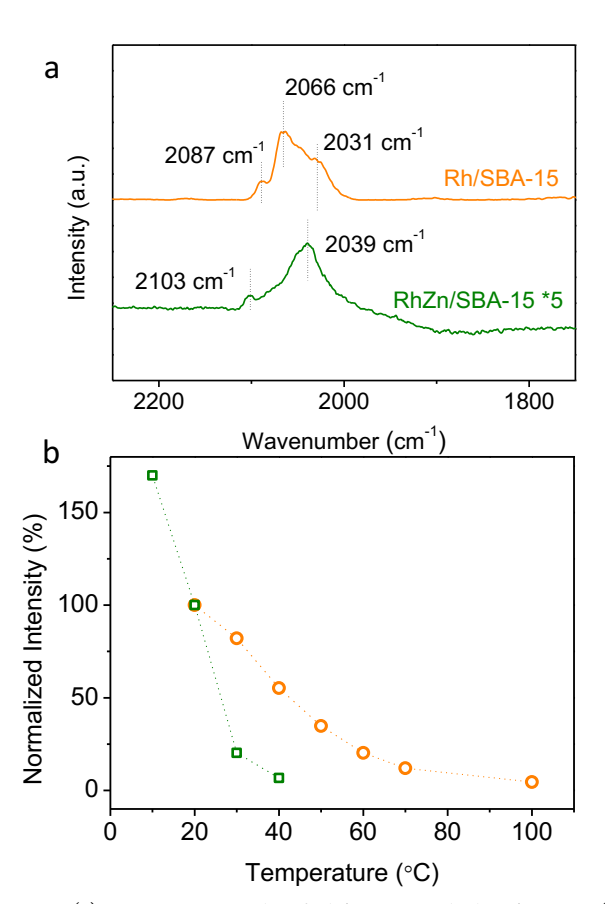


Figure 3. (a) CO-DRIFTS results of Rh/SBA-15 and RhZn/SBA-15. (b) Temperature-dependent evolution of the CO adsorption peak strength for Rh/SBA-15 and RhZn/SBA-15. Data for Rh/SBA-15 and RhZn/SBA-15 are color-coded as orange and green, respectively.

shown a chemoselectivity of near 100% to aldehydes. In comparison with Wilkinson's catalyst, RhZn/SBA-15 in general exhibits 2-3 times higher TOF at *ca.* 10% conversion, indicating that its enhanced

hydroformylation activity can be achieved on a variety of common substrates.

Diffuse reflectance infrared Fourier transform spectroscopy (DRIFTS) with CO as a probing molecule provides key information about the molecular adsorption behavior on Rh and RhZn surfaces. As shown in Figure 3a, CO on Rh surface exhibits two characteristic peaks of geminal Rh⁺(CO)₂ species at 2087 and 2031 cm⁻¹, as well as a peak of atop-adsorbed CO at 2066 cm^{-1.31-32} On the RhZn surface, however, the atop CO peak red-shifts to 2039 cm⁻¹. We performed density functional theory (DFT) calculations of CO vibrational modes at varying coverage on Rh(111) and RhZn(110) (see Table S4). These show a red-shift of roughly 10 cm⁻¹ due to a decrease in coverage from 0.50 ML to 0.25 ML, and an additional red-shift of roughly 10 cm⁻¹ due to the change from Rh(111) to RhZn(110). These calculations suggest a combination of effects from surface electronic states and adsorbate coverage on the observed C-O stretch. A temperature-programmed desorption study using DRIFTS³³ further reveals the CO peak shifts to low wavenumber with the increase of temperature on Rh surface, indicating the removing of CO dipole-dipole coupling with the decrease of CO coverage (Figure S9). Figure 3b shows the remaining amount of adsorbed CO at elevated temperatures, normalized by the CO coverage at 20 °C. CO fully desorbs from the Rh and RhZn surface at around 100 and 40 °C, respectively, marking a significantly lower adsorption strength of CO on RhZn surface. The weak CO adsorption on RhZn could leave more Rh sites for C=C and H₂ adsorption and facilitate the generation and desorption of product species, leading to the enhanced hydroformylation activity.

We performed a mechanistic study using DFT to obtain fundamental insights into the catalytic hydroformylation process. First, we calculated the surface energies of various low-index RhZn facets to identify those most favored under vacuum and under the synthesis and reaction conditions. These calculations included the clean surface, the surface with adsorbed H* (representing the synthesis conditions), and the surface with adsorbed CO* (representing the reaction conditions); these results are summarized in Figure 4a-b and Tables S5-S6. We did not perform calculations for a large number of possible surface coverages, which would enable a more quantitative analysis of the

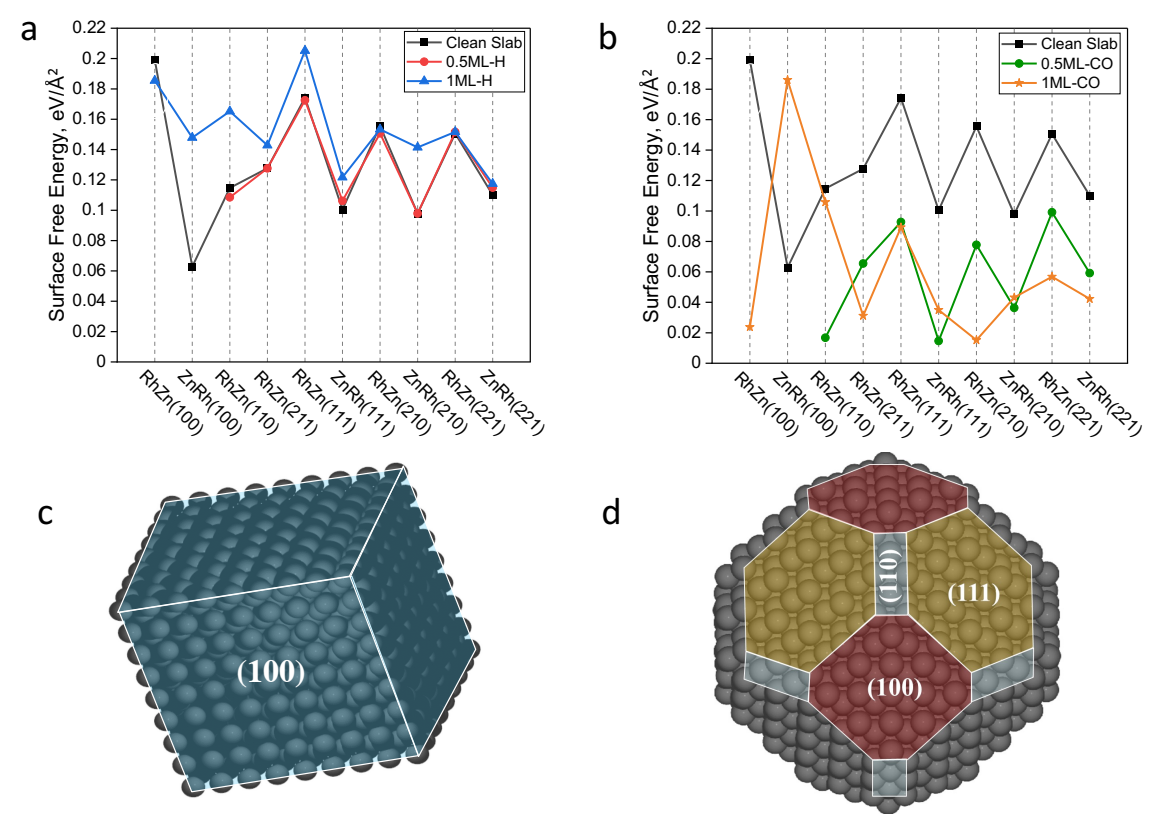


Figure 4. Surface free energies of bimetallic modeled surfaces under (a) catalyst synthesis conditions (500 °C and 1 atm H_2) and (b) reaction conditions (100 °C and 1 atm H_2 /CO). The corresponding surface coverage on each of the top and bottom slab surfaces is noted in the legend. Note that the primitive unit cells for RhZn(100) and ZnRh(100) have only one adsorption site so only one coverage is shown. (c) Wulff construction of a bimetallic RhZn nanocrystal under the synthesis conditions, showing the exposed ZnRh(100) planes. (d) Wulff construction under reaction conditions, showing relative stabilization of the ZnRh(111), RhZn(100), and RhZn(110) facets.

facets presented, but rather focused on obtaining first-order insights to qualitatively determine which facets are most likely to present in the reactive environment.

Our results show that Zn-rich terminations are preferentially exposed in vacuum (first column of Table S5); ZnRh(100), which only exposes Zn atoms, has the lowest surface energy of 0.063 eV/Å². The clean ZnRh(100) surface is still the lowest energy configuration under the synthesis conditions, as shown in Figure 4a, due to the unfavorable adsorption of H* on Zn and the inability of H* to substantially stabilize surface Rh atoms. The corresponding nanoparticle shape predicted by Wulff construction under the synthesis conditions is cubic, dominated by ZnRh(100) planes (Figure 4c). In contrast, Rhcontaining facets are substantially stabilized by CO* (Table S6). We therefore calculate that substantial nanoparticle re-faceting is energetically favorable under reaction conditions due to the stabilization of facets such as ZnRh(111), RhZn(100), and RhZn(110). The corresponding Wulff shape (Figure 4d) highlights the corresponding increase in those facets at equilibrium. We do not dwell on quantifying the relative exposures of each facet, in the absence of a more rigorous set of surface coverage data as well as the kinetics of restructuring. However, we note that selected studies of Rh/Zn segregation (performed by interchanging Rh and Zn atoms) were found to be unfavorable even in the presence of adsorbates due to the strong Rh-Zn interaction (Table S7).

Subsequently, we evaluated styrene hydroformylation energetics on energetically favored surfaces under these conditions (Figure 5).

The considered surfaces include those that are primarily Zn-terminated (sometimes with available Rh sites) such as ZnRh(100) and ZnRh(111) as well as the stoichiometrically balanced RhZn(110) surface. The Rh(111) surface was also considered as a reference to understand the thermodynamic and kinetic effects of including Zn on calculated energetics. We note that the RhZn(100) surface is also favorable under reaction conditions; however, this surface is anticipated to exhibit properties qualitatively similar to Rh(111) (overbinding, as discussed below), since only Rh atoms are exposed. The RhZn(210) surface, a stepped surface, is also relatively low-energy. Stepped features implicitly appear in our Wulff construction, though we did not evaluate their detailed energetics as we anticipate they may be poisoned by the particularly strong CO binding observed on the Rh sites (more than 0.3 eV stronger than on any other surface, Table S8). We then evaluated the energetics of styrene hydroformylation to the corresponding linear and branched products on each surface. We considered three sequential reaction steps (Figure S11), as done in a previous study¹² of hydroformylation, for each of the linear and branched pathways: addition of H*, addition of CO*, and the final addition of H* to form the product.

All hydrocarbon species are more strongly adsorbed on Rh(111) than on mixed Rh-Zn planes, as the presence of Zn weakens the adsorbate-surface interactions. The adsorption strength indeed is related to the amount of surface Zn (example adsorption free energies given for styrene): Zn-terminated surfaces such as ZnRh(100) (+0.34 eV) and ZnRh(111) (+0.08 eV) bind species weakly,

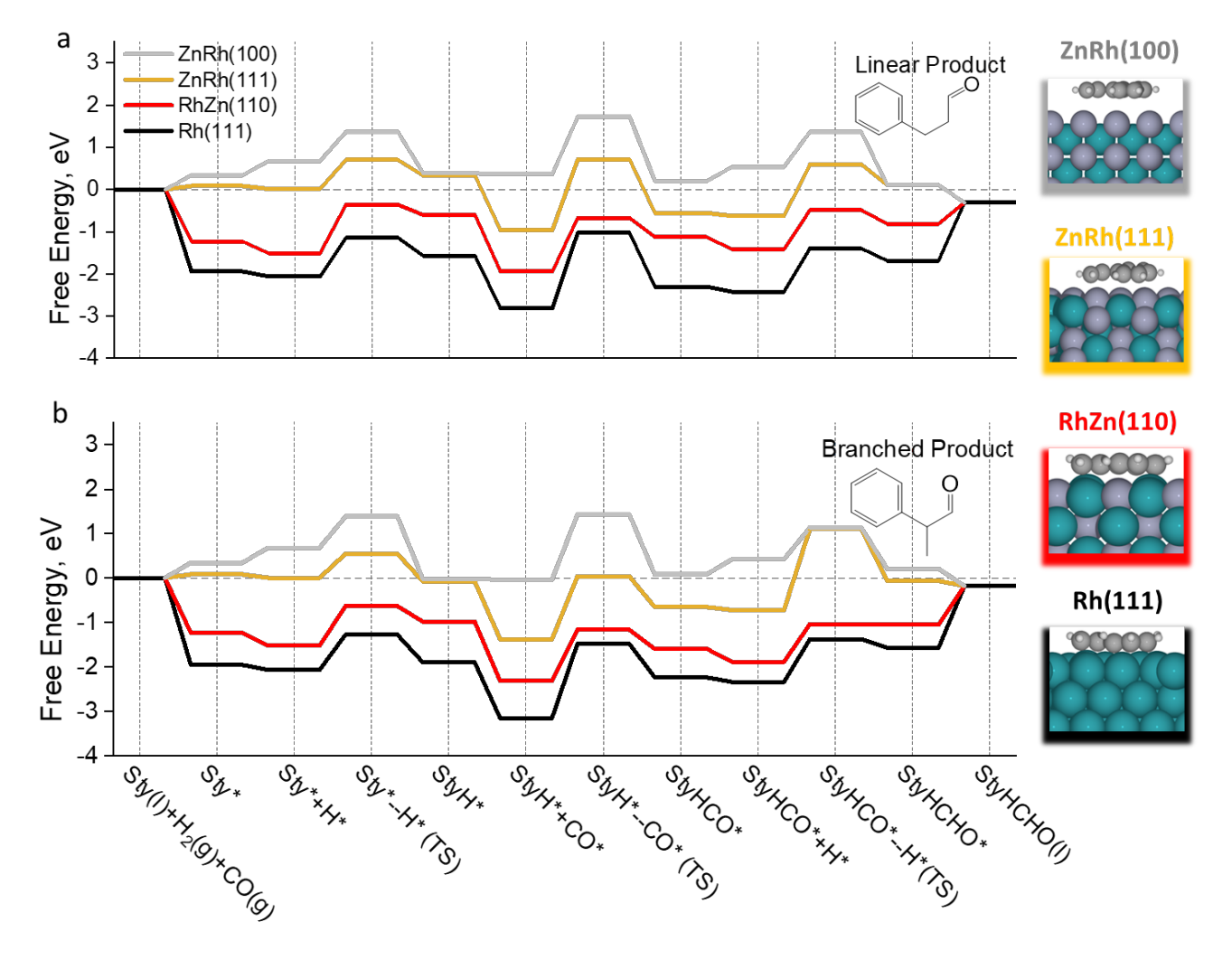


Figure 5. Free energy diagram for styrene hydroformylation via the (a) linear and (b) branched product pathways at 100 °C and 1 atm on the surfaces considered in this study. Note: all coadsorbed states correspond to infinite separation between adsorbed species. At the right are the most stable adsorption configurations of adsorbed styrene (side view) on the respective surfaces. Atom colors for adsorbed species: C (grey), H (white), Zn (light purple) and Rh (green).

RhZn(110) (-1.23 eV) has intermediate binding strength due to the accessibility of some surface Rh sites, and Rh(111) (-1.95 eV) binds most strongly. These variations have substantial impacts on reaction energetics and transition state formation, as discussed in the following paragraphs. Free energy diagrams and their respective energies for each surface are presented in the SI as Figures S12-S15 and Tables S9-S12. All activation energies are found in Table S13.

The strong binding of species on Rh(111) is likely to lead to high surface coverage, thereby reducing the turnover of catalytic sites. Rh(111) also demonstrates the highest activation energy barriers of the surfaces considered, with a maximum barrier of 1.79 eV along the linear product pathway and 1.67 eV along the branched pathway. This suggests the unsuitability of pure Rh catalysts is due to both unfavorable strong binding and sluggish kinetics. It is worth noting that the activation energies for CO addition are particularly high on Rh(111) in comparison with the other surfaces, while the H-addition steps are generally consistent with those on the intermetallic surfaces (Table S13).

On the other hand, the ZnRh(100) surface dominated by exposed Zn atoms has difficulty in adsorbing and activating reactive species. As shown in Figure 5, the energy landscape on ZnRh(100) generally falls above the reference energies, indicating unfavorable binding of adsorbed species (styrene, CO, H) on the Zn sites. Notably, the activation energies for elementary steps are lower than those on Rh(111) (maximum barriers of 1.43 and 1.47 eV for the linear and branched products, respectively); however, these are higher than for other surfaces, and the anticipated low coverage makes it unlikely to contribute significant activity.

ZnRh(111) and RhZn(110), which both present a mix of Rh and Zn surface sites, present more interesting surface energetics that suggest the possibility of reasonable activity. ZnRh(111) binds styrene and hydrogen more strongly than ZnRh(100) due to the presence of some surface Rh; this binding has a free energy nearly zero relative to the reference states. The binding of CO is much stronger to the Rh sites than to the Zn sites on ZnRh(100) and is consistent with binding to Rh sites on other surfaces. While these binding strengths overall may appear most favorable for the hydroformylation reaction, the

relatively strong binding of CO compared to styrene may limit the availability of sites for styrene adsorption and thereby inhibit the rate. Further, the maximum activation energies calculated for ZnRh(111) (1.68 and 1.82 eV for the linear and branched pathways, respectively) likely renders this surface relatively inactive. These high barriers likely stem from the isolated Rh sites and difficulty in H- and CO-attack across the geometric features of this Zn-rich surface.

RhZn(110), which presents a 1:1 ratio of surface Rh and Zn sites, offers more moderate binding strength of the hydrocarbon species, with adsorption energies more similar to Rh(111) than to the Zndominated surfaces. Its binding strength of CO is relatively similar to that of other surfaces. Although this binding could lead to significantly higher overall surface coverage than that observed on the Znrich surfaces, this relative enhancement of styrene binding could facilitate the competition of styrene with CO for available surface sites in the event that CO poisons Rh sites on other surfaces. Most significantly, the maximum activation energies (1.27 and 1.16 eV for the linear and branched pathways, respectively) are substantially lower than those for ZnRh(111). The rate constants (from a typical Arrhenius expression) corresponding to these barriers are more than five orders of magnitude higher on RhZn(110) than on ZnRh(111), suggesting a significant advantage of that surface in activating bonds and facilitating CO- and H-attack. The RhZn(110) surface thereby demonstrates an interesting balance whereby the Zn atoms are sufficient to weaken binding and reduce potential for poisoning relative to Rh(111), while the rows of Rh atoms provide sufficient bond activation and transition state stabilization to yield lower reaction barriers than calculated on the Zn-rich surfaces.

We also attempted to obtain computational insights into the regioselectivity of RhZn, as our experimental results did not demonstrate a clear preference for either the linear or branched products. We define the difference of the maximum activation energy between the linear and branched pathways ($\Delta E_{a,max}$) as a rough descriptor of anticipated activity along each pathway (Figure 6 and Table S14); positive values of $\Delta E_{a,max}$ show preference to the branched pathway while negative values promote the linear product. The strong-binding Rh(111) surface, which presents an isotropic distribution of Rh atoms, demonstrates an $\Delta E_{a,max}$ value of 0.12 eV. This suggests similarly favored transition states (TSs) for the attack of CO molecule to the substrate along the linear and branched pathway (1.79 eV for linear vs. 1.67 eV for branched, Table S14), which is expected due to the isotropic nature of the surface (Figure S16a). Incorporation of Zn metal in the RhZn(110) surface results in rows of Rh atoms separated by rows of Zn atoms. This surface shows a $\Delta E_{a,max}$ value of 0.11 eV. The addition of the CO molecule on Rh sites has a slightly more favored TS along the branched pathway; CO attack to the internal alkenyl is promoted by steric repulsion of the terminal methyl group exposing internal alkenyl towards the surface to more readily form the branched product (Figure S16b). On the Zn-dominated ZnRh(111) surface, $\Delta E_{a.max}$ is -0.14 eV favoring the linear pathway. The primary cause of this is the high barrier required for hydrogen diffusion via a long Rh-Rh bridge to attack the internal carbonyl in the transition state (Figure S16c). However, we note that the barriers for these steps (1.68 eV for linear vs. 1.82 eV for branched, Table S14) are sufficiently high that ZnRh(111) may be less active than other facets of this study. Finally, the ZnRh(100) surface, which presents no access to Rh atoms, shows $\Delta E_{a,max}$ value of -0.04 eV favoring the linear product. As already mentioned in this paper, the weak binding strength of the ZnRh(100) surface is unlikely to be capable of adsorbing sufficient reaction species; similar to the isotropic Rh(111) surface, the TS

energies are relatively similar (1.43 eV for linear vs. 1.47 eV for branched, Table S14) along the linear and branched pathway due to a dearth of Rh atoms.

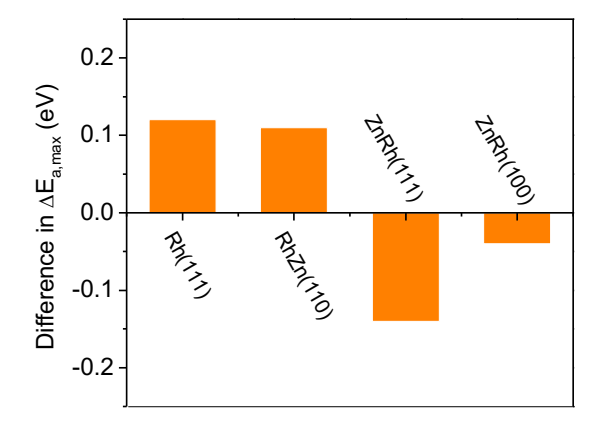


Figure 6. The calculated difference in maximum barrier along the linear and the branched reaction pathways for the hydroformylation process to occur on studied Rh and screened RhZn facets under reaction conditions.

Our Wulff construction of the nanoparticles under reaction conditions identified ZnRh(111) as majority facet, with some amounts of RhZn(110). Qualitatively, we anticipate these may be responsible for the mixed regioselectivity observed experimentally, noting that RhZn(110) should likely have the highest activity favoring the branched product, according to the Sabatier analysis and reaction barriers discussed above, while ZnRh(111) should have higher exposure but lower activity favoring the linear product.

CONCLUSION

In summary, we developed a series of Rh-based iNPs catalysts supported on mesoporous SBA-15. Applied to heterogeneous hydroformylation of styrene, the RhZn/SBA-15 nanocatalyst stands out with an outstanding TOF of 3090 h⁻¹, around three times higher than that of the homogeneous Wilkinson's catalyst (966 h⁻¹) under the same condition. We demonstrate that the RhZn/SBA-15 catalyst is recyclable and generally active for a range of olefin substrates, marking it a successful attempt to heterogenize the hydroformylation reaction. CO-DRIFTS studies confirmed the weak adsorption of CO on RhZn than Rh surfaces. DFT calculations revealed detailed insights into the hydroformylation mechanisms for branched and linear product formation on various intermetallic surfaces. RhZn(110), which presents a mixed Rh-Zn surface composition, was identified as the most likely active facet due to its intermediate binding strength of intermediates and relatively low activation energies. The surface chemistry observed in this study, which arises from geometric effects of inactive Zn rather than through strong modification of Rh electronic properties, opens the opportunity for surface science and catalytic chemistry to design feasible heterogeneous catalytic systems under the reaction environment. This could be one major advantage of mixed surfaces of intermetallic compounds in promoting hydroformylation reaction. This finding not only paves a way to apply heterogeneous hydroformylation to industrial chemical synthesis but also sheds light on the rational design of well-defined heterogeneous catalysts in order to bridge heterogeneous and homogeneous catalysis.

ASSOCIATED CONTENT

Supporting Information

The Supporting Information is available free of charge on the ACS Publications website.

Synthesis and additional characterization of the RhZn/SBA-15 catalyst, comparison of various Rh-based intermetallic nanoparticles, reaction optimization, comparison with literature, additional CO-DRIFTS results, detailed DFT calculation methods and results. (PDF) This material is available free of charge via the Internet at http://pubs.acs.org.

AUTHOR INFORMATION

Corresponding Author

* Wenyu Huang - Department of Chemistry, Iowa State University and US Department of Energy Ames Laboratory, Ames, IA 50011, United States.

Email: whuang@iastate.edu

* Luke Roling - Department of Chemical and Biological Engineering, Iowa State University, Ames, IA 50011, United States. Email: roling@iastate.edu

Author Contributions

The manuscript was written through contributions of all authors. All authors have given approval to the final version of the manuscript.

ACKNOWLEDGMENT

This work is partially supported by NSF grant CHE-2108306/2108307 and Trapp award from Iowa State University. We thank Tao Ma for assistance in STEM imaging at Ames Laboratory Sensitive Instrument Facility. We thank Matt Besser for the use of the X-ray diffractometer. We thank Zhicheng Luo and Aaron Sadow for the use of a special gas cylinder. LTR acknowledges support from the Michael and Denise Mack Faculty Fellowship.

REFERENCES

- (1) Tudor, R.; Shah, A., Industrial Low Pressure Hydroformylation: Forty-Five Years of Progress for the LP Oxo(SM) Process. *Johnson Matthey Technol. Rev.* **2017**, *61* (3), 246-256.
- (2) Evans, D.; Osborn, J. A.; Wilkinson, G., Hydroformylation of alkenes by use of rhodium complex catalysts. *J. Chem. Soc. A* **1968**, 3133-3142.
- (3) Brown, C. K.; Wilkinson, G., Homogeneous hydroformylation of alkenes with hydridocarbonyltris-(triphenylphosphine)rhodium(I) as catalyst. *J. Chem. Soc. A* **1970**, (0), 2753-2764.
- (4) Franke, R.; Selent, D.; Borner, A., Applied Hydroformylation. *Chem. Rev.* **2012**, *112* (11), 5675-5732.
- (5) Sun, Z.; Wang, Y.; Niu, M.; Yi, H.; Jiang, J.; Jin, Z., Poly(ethylene glycol)-stabilized Rh nanoparticles as efficient and recyclable catalysts for hydroformylation of olefins. *Catal. Commun.* **2012**, *27*, 78-82.
- (6) Tan, M.; Yang, G.; Wang, T.; Vitidsant, T.; Li, J.; Wei, Q.; Ai, P.; Wu, M.; Zheng, J.; Tsubaki, N., Active and regioselective rhodium catalyst supported on reduced graphene oxide for 1-hexene hydroformylation. *Catal. Sci. Technol.* **2016**, *6* (4), 1162-1172.
- (7) Shi, Y.; Hu, X.; Zhu, B.; Wang, S.; Zhang, S.; Huang, W., Synthesis and characterization of TiO2 nanotube supported Rh-nanoparticle catalysts for regioselective hydroformylation of vinyl acetate. *RSC Adv.* **2014**, 4 (107), 62215-62222.
- (8) Sordelli, L.; Guidotti, M.; Andreatta, D.; Vlaic, G.; Psaro, R., Characterization and catalytic performances of alkali-metal promoted Rh/SiO2 catalysts for propene hydroformylation. *J. Mol. Catal. A: Chem.* **2003**, 204-205, 509-518.
- (9) Hou, C.; Zhao, G.; Ji, Y.; Niu, Z.; Wang, D.; Li, Y., Hydroformylation of alkenes over rhodium supported on the metal-organic framework ZIF-8. *Nano Research* **2014**, *7* (9), 1364-1369.

- (10) Zhang, J.; Sun, P.; Gao, G.; Wang, J.; Zhao, Z.; Muhammad, Y.; Li, F., Enhancing regioselectivity via tuning the microenvironment in heterogeneous hydroformylation of olefins. *J. Catal.* **2020**, 387, 196-206.
- (11) Lang, R.; Li, T.; Matsumura, D.; Miao, S.; Ren, Y.; Cui, Y.-T.; Tan, Y.; Qiao, B.; Li, L.; Wang, A.; Wang, X.; Zhang, T., Hydroformylation of Olefins by a Rhodium Single-Atom Catalyst with Activity Comparable to RhCl(PPh3)3. *Angew. Chem. Int. Ed.* **2016**, *55* (52), 16054-16058.
- (12) Wang, L. B.; Zhang, W. B.; Wang, S. P.; Gao, Z. H.; Luo, Z. H.; Wang, X.; Zeng, R.; Li, A. W.; Li, H. L.; Wang, M. L.; Zheng, X. S.; Zhu, J. F.; Zhang, W. H.; Ma, C.; Si, R.; Zeng, J., Atomic-level insights in optimizing reaction paths for hydroformylation reaction over Rh/CoO single-atom catalyst. *Nat. Commun.* **2016**, *7*.
- (13) Ryoo, R.; Kim, J.; Jo, C.; Han, S. W.; Kim, J.-C.; Park, H.; Han, J.; Shin, H. S.; Shin, J. W., Rare-earth-platinum alloy nanoparticles in mesoporous zeolite for catalysis. *Nature* **2020**, *585* (7824), 221-224.
- (14) Ye, T.-N.; Lu, Y.; Xiao, Z.; Li, J.; Nakao, T.; Abe, H.; Niwa, Y.; Kitano, M.; Tada, T.; Hosono, H., Palladium-bearing intermetallic electride as an efficient and stable catalyst for Suzuki cross-coupling reactions. *Nat. Commun.* **2019**, *10* (1), 5653.
- (15) Dasgupta, A.; Rioux, R. M., Intermetallics in catalysis: An exciting subset of multimetallic catalysts. *Catal. Today* **2019**, 330, 2-15.
- (16) Studt, F.; Abild-Pedersen, F.; Bligaard, T.; Sorensen, R. Z.; Christensen, C. H.; Norskov, J. K., Identification of non-precious metal alloy catalysts for selective hydrogenation of acetylene. *Science* **2008**, *320* (5881), 1320-1322.
- (17) Furukawa, S.; Komatsu, T., Intermetallic Compounds: Promising Inorganic Materials for Well-Structured and Electronically Modified Reaction Environments for Efficient Catalysis. ACS Catal. **2017**, 7 (1), 735-765.
- (18) Pei, Y.; Zhang, B.; Maligal-Ganesh, R. V.; Naik, P. J.; Goh, T. W.; MacMurdo, H. L.; Qi, Z.; Chen, M.; Behera, R. K.; Slowing, I. I.; Huang, W., Catalytic properties of intermetallic platinum-tin nanoparticles with non-stoichiometric compositions. *J. Catal.* **2019**, *374*, 136-142.
- (19) Gamler, J. T. L.; Ashberry, H. M.; Skrabalak, S. E.; Koczkur, K. M., Random Alloyed versus Intermetallic Nanoparticles: A Comparison of Electrocatalytic Performance. *Adv. Mater.* **2018**, *30* (40), 1801563.
- (20) Ota, A.; Kröhnert, J.; Weinberg, G.; Kasatkin, I.; Kunkes, E. L.; Ferri, D.; Girgsdies, F.; Hamilton, N.; Armbrüster, M.; Schlögl, R.; Behrens, M., Dynamic Surface Processes of Nanostructured Pd2Ga Catalysts Derived from Hydrotalcite-Like Precursors. ACS Catal. 2014, 4 (6), 2048-2059.
- (21) Feng, Q. C.; Zhao, S.; Wang, Y.; Dong, J. C.; Chen, W. X.; He, D. S.; Wang, D. S.; Yang, J.; Zhu, Y. M.; Zhu, H. L.; Gu, L.; Li, Z.; Liu, Y. X.; Yu, R.; Li, J.; Li, Y. D., Isolated Single-Atom Pd Sites in Intermetallic Nanostructures: High Catalytic Selectivity for Semihydrogenation of Alkynes. *J. Am. Chem. Soc.* **2017**, *139* (21), 7294-7301.
- (22) Chen, M.; Yan, Y.; Gebre, M.; Ordonez, C.; Liu, F.; Qi, L.; Lamkins, A.; Jing, D.; Dolge, K.; Zhang, B.; Heintz, P.; Shoemaker, D. P.; Wang, B.; Huang, W., Thermal Unequilibrium of PdSn Intermetallic Nanocatalysts: From In Situ Tailored Synthesis to Unexpected Hydrogenation Selectivity. *Angew. Chem. Int. Ed.* **2021**, *60* (33), 18309-18317.
- (23) Zhao, E. W.; Maligal-Ganesh, R.; Xiao, C.; Goh, T. W.; Qi, Z.; Pei, Y.; Hagelin-Weaver, H. E.; Huang, W.; Bowers, C. R., Silica-Encapsulated Pt-Sn Intermetallic Nanoparticles: A Robust Catalytic Platform for Parahydrogen-Induced Polarization of Gases and Liquids. *Angew. Chem. Int. Ed.* **2017**, *56* (14), 3925-3929.
- (24) Pei, Y.; Chen, M.; Zhong, X.; Zhao, T. Y.; Ferrer, M.-J.; Maligal-Ganesh, R. V.; Ma, T.; Zhang, B.; Qi, Z.; Zhou, L.; Bowers, C. R.; Liu, C.; Huang, W., Pairwise semi-hydrogenation of alkyne to cis-alkene on platinum-tin intermetallic compounds. *Nanoscale* **2020**, *12* (15), 8519-8524.
- (25) Maligal-Ganesh, R. V.; Xiao, C. X.; Goh, T. W.; Wang, L. L.; Gustafson, J.; Pei, Y. C.; Qi, Z. Y.; Johnson, D. D.; Zhang, S. R.; Tao, F.; Huang, W. Y., A Ship-in-a-Bottle Strategy To Synthesize Encapsulated Intermetallic Nanoparticle Catalysts: Exemplified for Furfural Hydrogenation. ACS Catal. 2016, 6 (3), 1754-1763.
- (26) Feng, X.; Liu, J.; Zhang, P.; Zhang, Q.; Xu, L.; Zhao, L.; Song, X.; Gao, L., Highly coke resistant Mg–Ni/Al2O3 catalyst prepared via a novel magnesiothermic reduction for methane reforming catalysis with CO2: the unique role of Al–Ni intermetallics. *Nanoscale* **2019**, *11* (3), 1262-1272.

- (27) Liu, Z.; Jackson, G. S.; Eichhorn, B. W., PtSn Intermetallic, Core-Shell, and Alloy Nanoparticles as CO-Tolerant Electrocatalysts for H2 Oxidation. *Angew. Chem. Int. Ed.* **2010**, 49 (18), 3173-3176.
- (28) Anres, P.; Fossati, P.; Gaune-Escard, M.; Bros, J. P., Thermodynamics of the [Rh-In] system. *J. Alloys Compd.* **1998**, 266 (1), 241-246.
- (29) Massalski, T. B.; Okamoto, H.; International, A. S. M., Binary alloy phase diagrams. ASM International: Materials Park, Ohio, 1990.
- (30) Pearson, R. G., Absolute electronegativity and hardness: application to inorganic chemistry. *Inorg. Chem.* **1988**, 27 (4), 734-740.
- (31) Varga, E.; Pusztai, P.; Óvári, L.; Oszkó, A.; Erdőhelyi, A.; Papp, C.; Steinrück, H. P.; Kónya, Z.; Kiss, J., Probing the interaction of Rh, Co and bimetallic Rh–Co nanoparticles with the CeO2 support: catalytic materials
- for alternative energy generation. Phys. Chem. Chem. Phys. 2015, 17 (40), 27154-27166.
- (32) Zhu, H.; Li, Y.; Zheng, X., In-situ DRIFTS study of CeO2 supported Rh catalysts for N2O decomposition. *Appl. Catal. A* **2019**, *571*, 89-95.
- (33) Goh, T. W.; Tsung, C.-K.; Huang, W., Spectroscopy Identification of the Bimetallic Surface of Metal–Organic Framework-Confined Pt–Sn Nanoclusters with Enhanced Chemoselectivity in Furfural Hydrogenation. *ACS Appl. Mater. Interfaces* **2019**, *11* (26), 23254-23260.

Table of Contents artwork

